University of New Hampshire
University of New Hampshire Scholars' Repository

Center for Coastal and Ocean Mapping

Center for Coastal and Ocean Mapping

5-2014

Acoustic estimates of methane gas flux from the seabed in a 6000 km2 region in the Northern Gulf of Mexico

Thomas C. Weber
University of New Hampshire, Durham, thomas.weber@unh.edu

Larry A. Mayer
University of New Hampshire, larry.mayer@unh.edu

Kevin W. Jerram
University of New Hampshire, Durham, kevin.jerram@unh.edu

Jonathan Beaudoin
University of New Hampshire, Durham

Yuri Rzhanov
University of New Hampshire, Durham, Yuri.Rzhanov@unh.edu

Follow this and additional works at: https://scholars.unh.edu/ccom

Acoustic estimates of methane gas flux from the seabed in a 6000 km^2 region in the Northern Gulf of Mexico

Thomas C. Weber[1], Larry Mayer[1], Kevin Jerram[1], Jonathan Beaudoin[1], Yuri Rzhanov[1], and Dave Lovalvo[2]

[1]Center for Coastal and Ocean Mapping, University of New Hampshire, Durham, New Hampshire, USA, [2]NOAA Office of Exploration and Research, Silver Spring, Maryland, USA

Abstract Seeps of free methane gas escaping the seabed can be found throughout the ocean basins. To understand the role of methane gas seeps in the global carbon cycle—including both gas added to the atmosphere and that which is dissolved and potentially oxidized in the ocean volume—it is important to quantify the amount of methane escaping the seabed. Few large-scale mapping projects of natural methane seeps have been undertaken, however, and even among these, quantitative estimates of flux are rare. Here we use acoustic mapping techniques to survey 357 natural methane seeps in a large region (6000 km^2) of the northern Gulf of Mexico and outline a general approach for methane seep mapping using a combination of multibeam and split-beam echo sounders. Using additional measurements collected with a remotely operated vehicle (ROV) together with the acoustic mapping results, we estimate the total gas flux within the 6000 km^2 region to be between 0.0013 and 0.16 Tg/yr, or between 0.003 and 0.3% of the current estimates for global seabed methane seepage rates.

1. Introduction

Free methane gas has been widely observed to be escaping the seabed in the world's oceans from sources that are either of biogenic origin, typically in shallow sediments, or thermogenic origin in deep sediments [*Judd*, 2004]. After escaping the seabed, methane bubbles undergo a complicated upward journey toward the sea surface, involving the transfer of methane from the bubble into aqueous solution and the transfer of other gases (e.g., N_2, O_2) into the bubble [e.g., *McGinnis et al.*, 2006]. Several mechanisms potentially affect the gas transfer rate to/from methane bubbles during their ascent through the water column. Both laboratory and deep ocean experimental evidence supports the presence of a hydrate coating on the bubble wall if the bubble originates within the hydrate stability zone [e.g., *Maini and Bishnoi*, 1981; *Rehder et al.*, 2002; *Sauter et al.*, 2006; *Rehder et al.*, 2009], although the dissolution rate of naturally occurring hydrate-coated bubbles has not yet been quantified. It has also been suggested that oil coatings on methane bubbles provide a largely unaccounted-for mechanism that transports methane to the atmosphere in bubbles that would otherwise dissolve [*Solomon et al.*, 2009]. The reduction in hydrostatic pressure acts to increase the bubble size, increasing the surface area over which gas transfer can occur, while the surface tension at the bubble wall, which is affected by the presence of surfactants or adsorbed particulate material, increases the tendency for bubble dissolution [*Epstein and Plesset*, 1950]. All of these mechanisms must be understood to determine the eventual fate of free methane gas exiting the seabed.

Methane gas in bubbles that reach the surface is injected into the atmosphere where it has the potential to affect climate due to methane being a greenhouse gas. Dissolved methane gas that reaches the ocean mixed layer may also reach the atmosphere through equilibration at the ocean surface, although some of the dissolved methane may be microbially oxidized before this occurs [*Mau et al.*, 2007; *Reeburgh*, 2007]. To understand the role of methane gas seeps in the global carbon cycle—including gas added to the atmosphere and that which is dissolved and potentially oxidized in the ocean volume—it is important to both quantify the amount of methane escaping the seabed and to understand the transport of gas across the bubble boundary as it travels upward through the water column. In this work, we address the former using a combination of acoustic mapping techniques together with a limited number of remotely operated vehicle (ROV) dives to survey 357 natural methane seeps in a large region (6000 km^2) of the northern Gulf of Mexico.
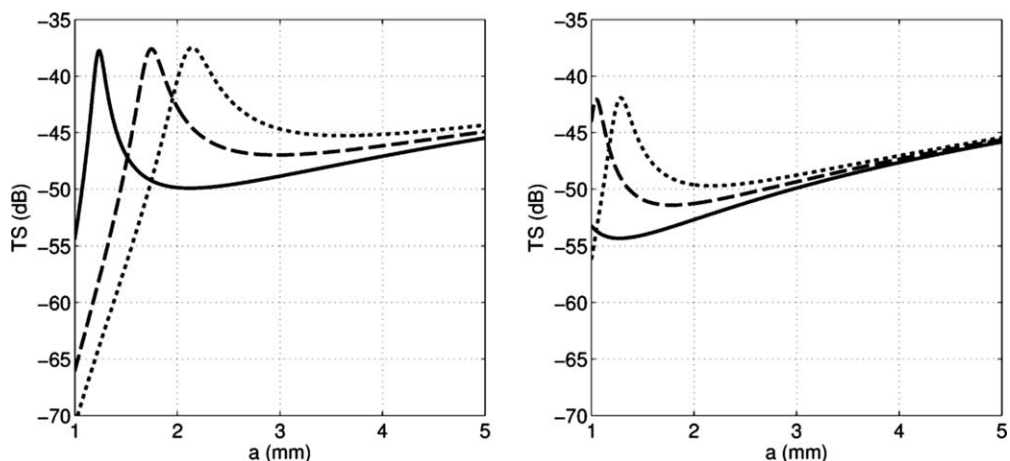
Figure 1. Modeled TS for bubbles at (left) 18 kHz and (right) 30 kHz for three different water depths: 500 m (solid line), 1000 m (dashed line), and 1500 m (dotted line).

The acoustic mapping techniques used here employ both a 30 kHz multibeam echo sounder (MBES) and an 18 kHz split-beam echo sounder (SBES). Both types of echo sounders have unique advantages: the wide swath of the MBES offers the potential for efficient mapping and localization of gas seeps and the SBES offers a well-established path to absolute acoustic measurements using standard calibration techniques [e.g., *Foote et al.*, 1987] and split-aperture processing techniques [*Burdic*, 1991].

Acoustic anomalies associated with gas seeps similar to the ones analyzed here have previously been observed by other investigators [e.g., *Merewether et al.*, 1985; *Dimitrov and Dontcheva*, 1994; *Hornafius et al.*, 1999; *MacDonald et al.*, 2002; *Heeschen et al.*, 2003; *Greinert et al.*, 2006; *Westbrook et al.*, 2009; *Greinert et al.*, 2010; *Schneider von Deimling et al.*, 2011; *Römer et al.*, 2012; *Kannberg et al.*, 2013]. These types of acoustic observations of gas seeps exploit a gas bubble's mechanical resonance and large acoustic impedance contrast with the surrounding seawater. The target strength (TS) of a single bubble can be calculated from the total scattering cross section of the bubble, σ, which is dependent on both the bubble size, a, and frequency of ensonification, f:

$$TS = 10 \log_{10} \frac{\sigma}{4\pi} = 10 \log_{10} \frac{a^2}{\left[\left(\frac{f_R}{f}\right) - 1\right]^2 + \delta^2} \qquad (1)$$

where f_R is the resonance frequency of the bubble and δ is a damping coefficient that incorporates energy losses in the vibrating bubble due to thermal dissipation, viscous losses in the fluid surrounding the bubble, and acoustic reradiation [*Clay and Medwin*, 1977]. The use of equation (1) assumes that the monopole resonance of the bubble dominates the scattered acoustic field (note that the wavelength at 18 kHz is approximately 8 cm, an order of magnitude large than the bubbles observed here) and also neglects changes in the acoustic response related to deformations in the bubble shape. Nonspherical bubbles have been shown to have changes in resonance frequency, peak scattering amplitude, and quality factor Q from that of a spherical bubble with the same volume, although small deformations may cause only minor effects (e.g., prolate spheroid air bubbles with an aspect ratio of 2 or less at, presumably, ambient pressure conditions show variations of only a few percent) [*Feuillade and Werby*, 1994]. For any nonspherical bubbles examined here, equation (1) is used to estimate the acoustic response and a is assumed to be the "effective" bubble radius given by the volume, v, of the bubble: $(3/4v)^{1/3}$. Figure 1 shows both 18 and 30 kHz TS models for single methane bubbles with radii between 1 and 5 mm, a typical size range for bubbles in methane seeps [e.g., *Leifer and MacDonald*, 2003; *Römer et al.*, 2012], using equation (1) and the formulation for f_R and δ given by *Clay and Medwin* [1977]. The scattering cross sections for collections of bubbles in gas seeps ensonified by SBES and MBES are usually assumed to be additive. In general, higher measurements of TS suggest a larger number of bubbles, although the resonant nature of bubbles can confound this generalization (i.e., a few bubbles excited near resonance can have the same TS as many bubbles excited away from their

resonance frequency). If the distribution of bubble sizes associated with a seep is known, or can be estimated, then TS measurements of a gas seep can be used to provide estimates of gas volume fraction.

In this work, seeps within a study area are identified and localized during a survey conducted from 22 August 2011 to 10 September 2011 using a 30 kHz MBES, producing an estimate of both the spatial distribution and number of seeps. A subset of these seeps were also acoustically characterized using a calibrated 18 kHz SBES, resulting in an estimate of the seep TS. These acoustic analyses are described in section 2. One of the seeps observed in 2011 was revisited in April 2012 with the same SBES and MBES, and was also visited with an ROV. During one ROV dive the bubble size distribution and rise velocity was calculated using a calibrated grid (described in section 3). The combination of calibrated SBES measurements and knowledge of the bubble size distribution and rise velocity made it possible to acoustically estimate the flux rate of gas escaping the seep. This flux rate estimate was then compared to a timed capture of the gas (i.e., a direct estimate of the flux rate) made with the ROV on a subsequent dive, providing some estimate of the accuracy of the acousto-optical measurements. Finally, the flux rate measurements were extrapolated to the entire 2011 survey area, using the acoustic observations as a constraint, in order to estimate bounds on the regional flux of methane gas. These estimates of the flux rate are described in section 4.

2. Acoustic Observations of Methane Seeps

Acoustic backscatter data were collected with both an 18 kHz Simrad EK60 SBES and a 30 kHz Kongsberg EM302 MBES during survey operations on board the NOAA Ship *Okeanos Explorer* in the northern Gulf of Mexico between 26 August 2011and 1 September 2011 and 6–9 September 2011. The survey covered 6000 km^2 (Figure 2), approximately 0.4% of the Gulf of Mexico basin, in water depths between 900 and 2600 m. Water temperatures over this depth range were observed to be as high as 5.4°C, at 900 m water depth, and as low as 4.3°C in the deeper waters (see supporting information), and suggest that the bubbles were originating within the hydrate stability zone based on the model of *Tishenko et al.* [2005]. During the survey, acoustic anomalies associated with natural seeps were observed in both the SBES and MBES (e.g., Figure 3). The SBES data typically show a much wider-looking seep than the MBES, which is a result of the wider SBES beam width (11°) as compared to the MBES (1°). When the SBES targets associated with gas seeps are processed using the SBES split-beam capability, targets are positioned to an accuracy that is commensurate with that of the narrow-beam width MBES [*Weber*, 2012].

The MBES data were manually scrutinized in order to localize the seabed sources of each seep, resulting in 573 observations of gas seeps during the survey. For each observation, the range/angle pair corresponding to the seabed source was identified and reduced to a georeferenced location using a processing path identical to that typically used for generating bathymetric soundings (e.g., accounting for vessel motion, sound refraction, etc.). Some of the MBES seep observations were thought to be repeat observations. Using an estimated system resolution of 1.7% of the water depth, which is the nominal seabed footprint for a 1° beam width, 357 observations of seeps were made from uniquely identifiable seabed locations (Figure 2), excluding seeps in the immediate vicinity of possible anthropogenic sources (e.g., leaky well heads and pipelines). Of the 357 observations of uniquely identifiable seeps, 54% were observed within 100 m of at least one other seep, 22% were observed within 100 m of at least two other seeps, and 8% were observed within 100 m of at least three other seeps.

Most of the seeps were observed on the edges of large domed structures caused by salt diapirism. Faults associated with the outer edges of the diapirs provide pathways for the leakage of deep trapped gas and other fluids to the seafloor [*Hood et al.*, 2002]. The geologic setting suggests that the seeps are largely comprised of methane (CH_4), although other gas constituents have been observed in relatively small quantities from hydrocarbons directly spilled into the deep ocean in the same area [e.g., *Kessler et al.*, 2011]. Gas samples were not collected from the seeps during this work, and it is assumed for the sake of the present work that the observed gas bubbles are comprised of methane alone. It should also be noted that past investigators have found evidence of oil slicks attributed to natural seeps in this region using synthetic aperture radar (SAR) imagery [*Garcia-Pineda et al.*, 2010]. There were no shipboard observations of surface oil slicks made during the present study, and follow-up site visits with the ROV detected no oil escaping the seabed at the few seep sites visited, but it should be noted that a comprehensive effort was not made to detect oil at either the ocean surface or bottom.
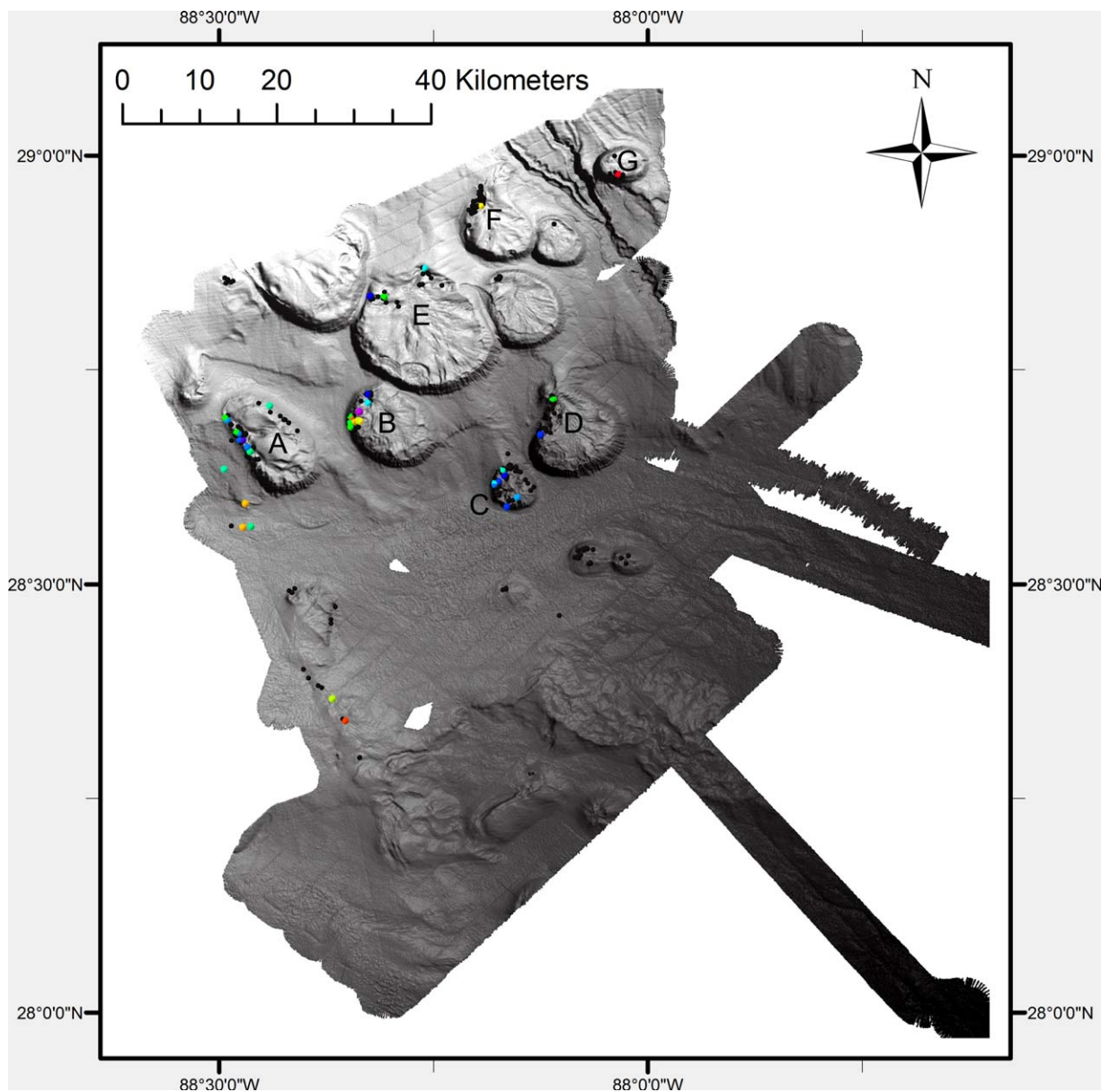
Figure 2. Bathymetry and seep observations in the northern Gulf of Mexico. Black dots indicate acoustic anomalies associated with gas seeps originating from the unique seabed locations, observed with MBES. Colored dots indicate gas seeps observed with SBES. Color represents the seep TS with warmer colors representing stronger seeps (red corresponds to a TS of −13 dB) and cooler colors representing weaker seeps (purple corresponds to a TS of −33 dB). Labeled domes include the (A) Biloxi Dome, (B) Gloria Dome, (C) Dauphin Dome, (D) Mobile Dome, (E) Mitchell Dome, (F) Horn Dome, and the (G) Pascagoula Dome.

A subset of the gas seeps observed with the MBES was simultaneously observed with the 18 kHz SBES, which was calibrated using a standard calibration sphere midway through the cruise following the procedure described by *Foote et al.* [1987]. Data collected with the 18 kHz SBES include time series of scattered acoustic power and electrical phase angles. These data were converted into apparent acoustic TS (TS modulated by the angular-dependent receiving sensitivity of the SBES, so that true TS is found on the SBES maximum response axis, or MRA, and apparently weaker TS are found at angles away from the MRA) and alongship and athwartship mechanical angles, using software developed by *Towler* [2013]. The only modification to the apparent TS predicted by Towler is a correction for the cumulative acoustic absorption that was estimated using expendable bathythermograph (XBT) and conductivity- temperature-depth (CTD) profiles collected during the cruise along with the absorption model of *Francois and Garrison* [1982]. It is
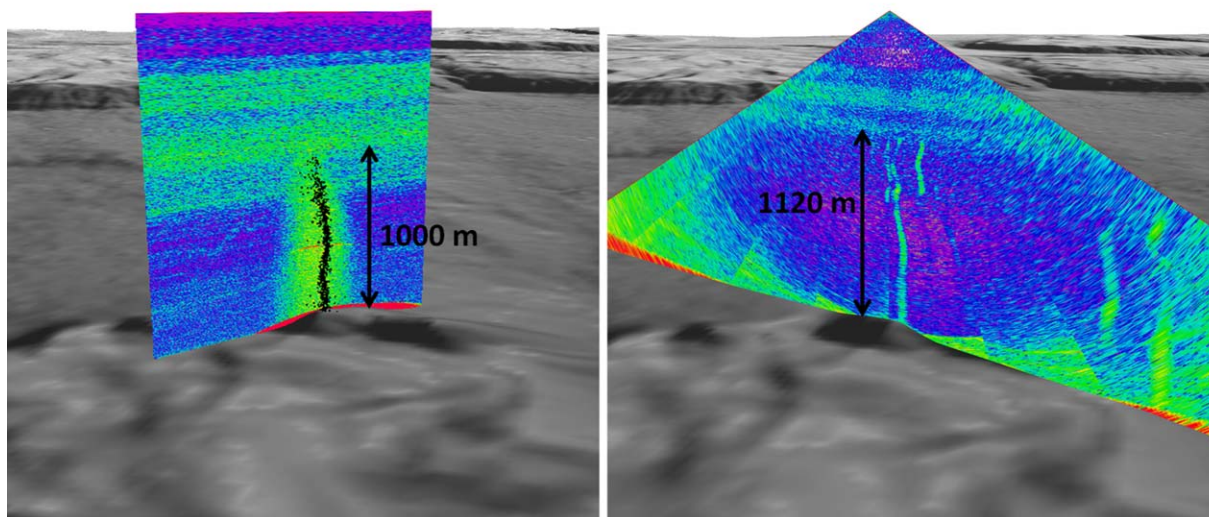
Figure 3. Acoustic anomalies associated with natural seeps observed with the (left) SBES (100 pings shown) and (right) MBES (one ping shown). These data were collected simultaneously on the northern side of the Dauphin Dome on 7 September 2011. Multiple seeps can be seen in the MBES data. The black dots overlaid on the SBES data represent the result of split-beam processing with the results averaged in 1 m deep bins (1–20 data values per bin).

important to note that the TS measurements reported here show the integrated response of the seep along the 4 ms pulse length (nominally 3 m in range accounting for two-way travel time).

Examples of the SBES data are shown in Figure 4 for seeps found on the Biloxi, Gloria, Mobile, and Pascagoula Domes. Due to the broad SBES beam width, the seep targets are observed for tens of pings as the vessel traverses over the seep. The alongship angle (Figure 4, column 2) monotonically decreases as the seep is first observed ahead of the ship, then underneath the ship, and then behind the ship. The athwartship angle (Figure 4, column 3) varies less than the alongship angle, and identifies whether the vessel passed to port, starboard, or directly over the seep. In addition to correcting the apparent TS for effects related to the SBES beam pattern, the alongship and athwartship angles can be used to position the seeps to an accuracy of a few tens of meters in water depths of over 1000 m [*Weber*, 2012].

The SBES data have been used to create vertical profiles of TS. To do so, acoustic anomalies associated with seeps are first identified in the raw data (e.g., Figure 4) by manual scrutiny. When a seep is observed, background noise adjacent to the seep (approximately 50 pings) is averaged to create a vertical profile of the average background noise. Targets associated with the seep are then identified using a depth-dependent threshold filter of 10 dB above the background noise profile. Each target is associated with an apparent TS value and two mechanical angles corresponding to the target direction in the alongship and athwartship directions (Figure 4, columns 2 and 3). Because targets located at angles off the beam MRA appear weaker than on-axis targets, the measurements of mechanical angle are used to adjust the apparent TS for the beam pattern modulation so that unbiased estimates of TS can be made (see supporting information). All TS measurements for unique seep observations are then averaged in depth bins of 20 m to create vertical profiles of seep TS. Note that these TS profiles integrate all bubbles that are present at any given depth in the 4 ms long acoustic pulse (equivalent to approximately 3 m, vertically) used by the SBES, and inherently assume that the bubbles are not changing appreciably over the 20 m depth window (roughly 100 s in the lifetime of the bubble).

Examples of vertical profiles of seep TS and background noise profiles are shown in Figure 5. The background noise is generally low below ∼1100 m, and often shows multiple peaks at shallower depths that are associated with reverberation from the deep scattering layer. The deep scattering layer is an assemblage of marine organisms [e.g., *Hopkins and Landcraft*, 1984] that scatter acoustic waves [*Clay and Medwin*, 1977], appearing as horizontal bands in TS data shown in Figure 4 and potentially masking the scattered return from any bubbles at the same depths. Despite the potential masking effect from the deep scattering layer, the TS profiles can be observed extending several 100s of meters upward from their seabed source,
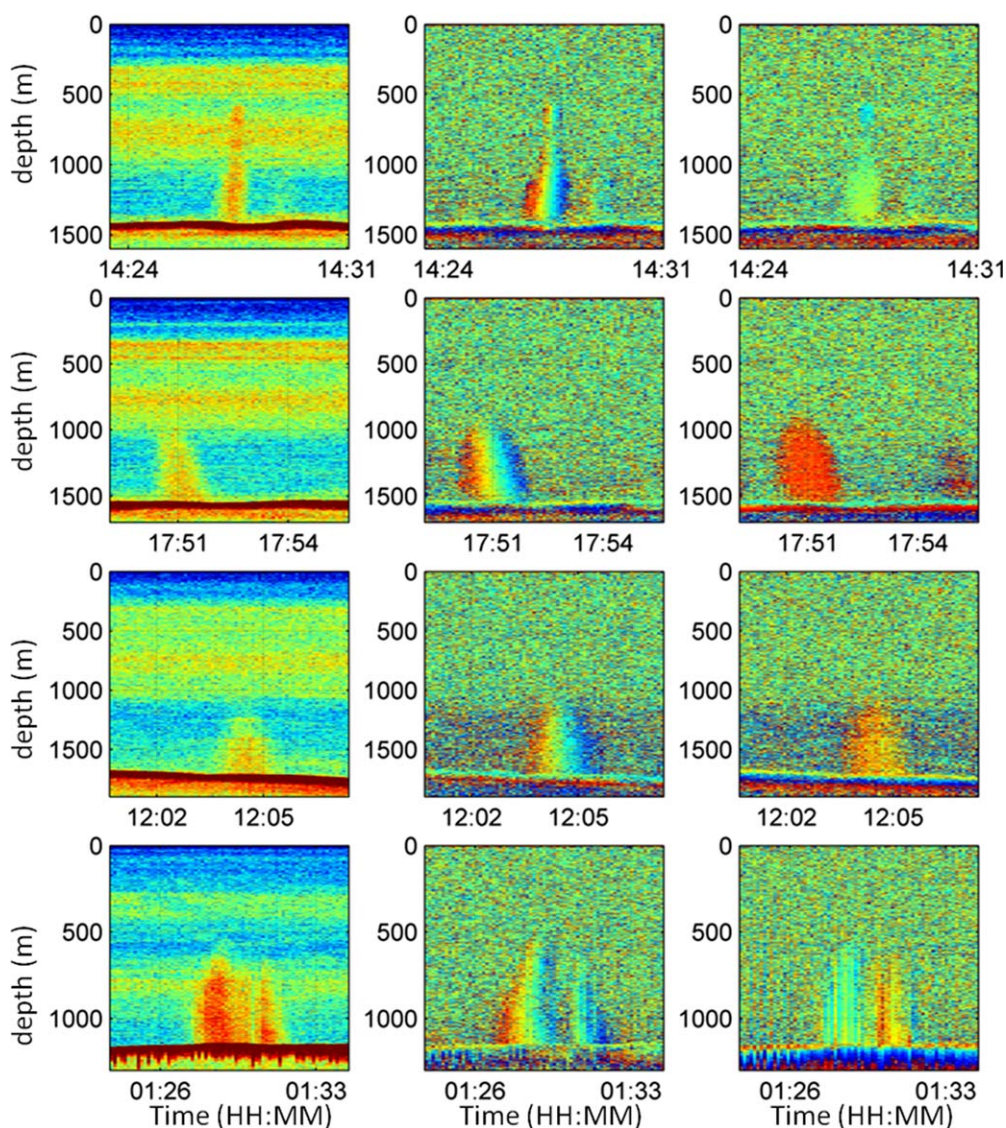
Figure 4. Examples of raw SBES data used to generate vertical TS profiles for seeps. (column 1) Apparent TS (uncorrected for the SBES beam pattern. (column 2) Alongship target mechanical angle. (column 3) Athwartship target mechanical angle. From top to bottom, these data correspond to the Biloxi Dome (30 August 2011), the Gloria Dome (30 August 2011), the Mobile Dome (7 September 2011), and the Pascagoula Dome (April 2012).

suggesting that there is some mechanism such as the presence of a hydrate coating on the bubble which is inhibiting bubble dissolution [see, e.g., *McGinnis et al.*, 2006]. However, the TS profiles in Figure 5 do not always exhibit the same depth-dependent behavior. For example, Figure 5G* shows a TS profile that decreases monotonically by 15 dB as the bubble rises from 800 to 550 m water depth. Assuming the gas to be steadily escaping the seep, the simplest explanation for this decrease in TS is that the bubbles are at or near resonance at 800 m water depth and reduce size as they rise through the water column, with the reduction in size occurring at a fast enough rate that bubble becomes smaller than the depth-dependent size of a resonating bubble at 18 kHz. In other SBES observations of seeps, the TS profile decays more slowly with depth (e.g., ~5 dB over a 600 m vertical ascent in B1). With TS observations at only one frequency, the cause for this reduced rate of TS decay is ambiguous and could be consistent with a gradual increase in bubble size as it rises, or a gradual decay in size of an initially resonant bubble. Similarly, TS profiles that are constant with depth are consistent with both a slight increase in bubble size during ascent for bubbles that are initially above resonance, or a slight decrease in bubble size during ascent for near-resonance bubbles.
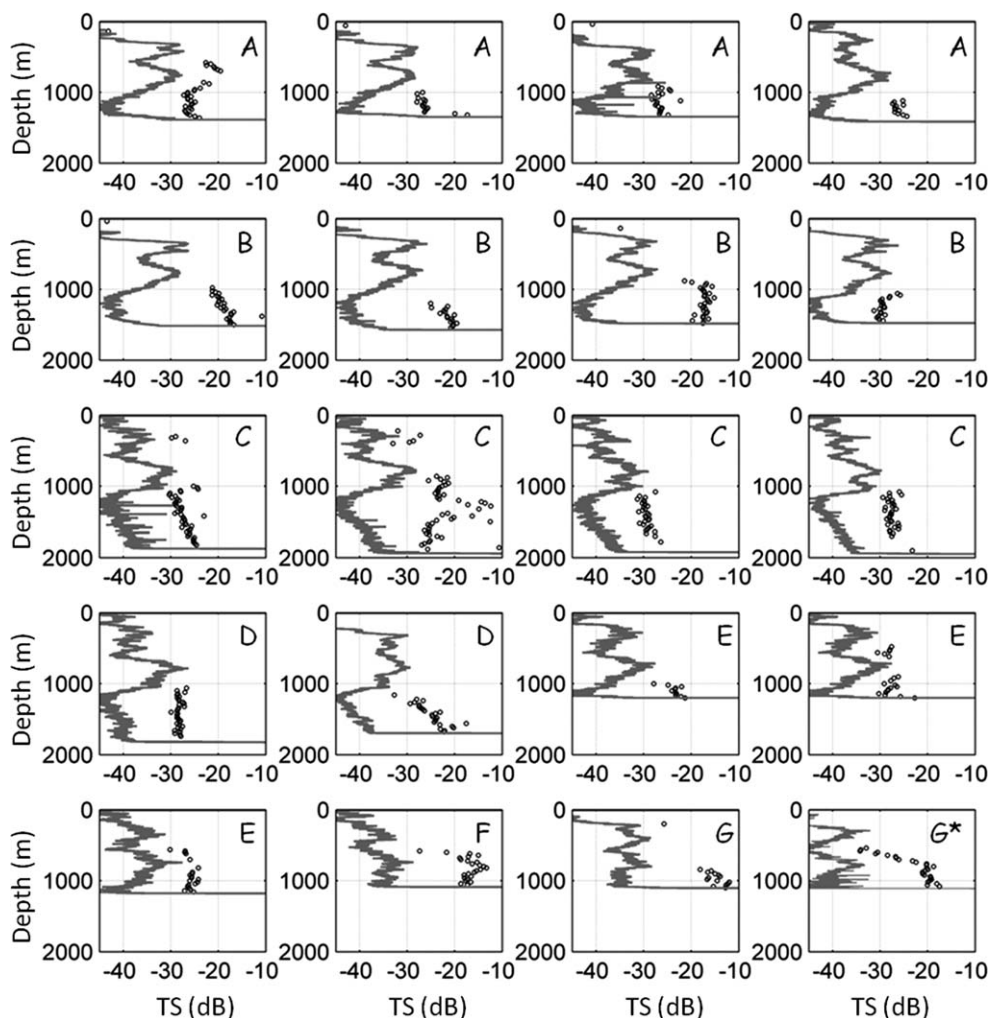
Figure 5. Acoustic profiles of TS for a subset of observed seeps (black dots), and background noise profiles at each location (gray lines, no beam pattern correction). This subset set shows seeps observed on the (A) Biloxi, (B) Gloria, (C) Dauphin, (D) Mobile, (E) Mitchell, (F) Horn, and (G) Pascagoula domes, with letters corresponding to locations shown in Figure 2. All observations were made in 2011 with the exception of G*, which was made in 2012.

3. ROV Observations of Bubble Size and Rise Velocity

In 2012, one of the seeps originally observed in 2011 on the Pascagoula dome was revisited with the same SBES (data from the revisit are shown in Figure 5G*) and MBES as well as an ROV. Estimates of bubble size were made during an ROV dive by placing a grid approximately 10 cm behind the seep (Figure 6). The grid was constructed with 2″ × 2″ squares (the laser dots in Figure 6 are separated by 10 cm) to help mitigate the effects of lens distortion. The distance between the camera and the center of the grid was 0.80 m, and so the bubbles are only 7/8th of their apparent size in the images due to the geometry of the field of view. Estimates of bubble sizes near the seabed were extracted from ROV camera data of the grid for times when there were no changes to camera focal length. For this work, the data with the highest zoom level were used, resulting in a horizontal pixel size of approximately 0.5 mm and a vertical pixel size of 1 mm after the video was deinterlaced. Video frames were captured at 30 frames/s (prior to deinterlacing).

When processing the video data, a background pattern used to determine grid locations was generated by averaging all frames. Bubbles were observed to be brighter than the background when appearing between gridlines, and darker than the background when overlapping a gridline. Bubbles were detected by differencing odd and even frames (separately) in the deinterlaced video. For the imagery used here, the rise speed of the bubbles was fast enough that the bubbles did not have overlapping locations in sequential frames. Pixels in the "difference image" at the gridline locations were multiplied by −1 in order to account
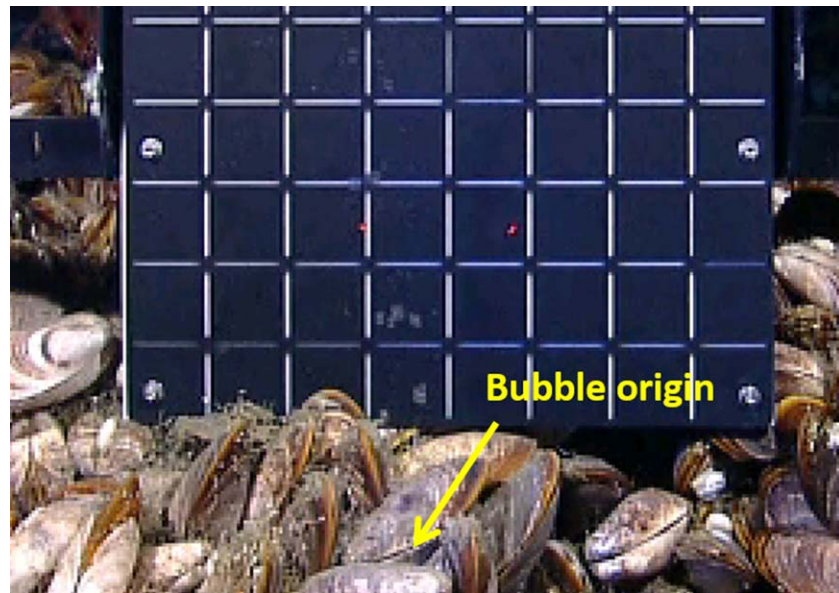
Figure 6. Grid used for estimating bubble sizes and positions with respect to the gas seep during measurements. The gas seep is estimated to be 10 cm in front of the grid.

for the opposite brightness of the background. A Canny edge detector was then applied to this modified difference image in order to identify the 1 pixel wide bubble perimeters. The Canny edge detector detects steep gradients in brightness, and in some instances where the gradient in brightness was gradual the bubble perimeter was not complete. In these instances, the perimeters were closed using a straight line. Each closed perimeter was classified with a unique ID. An example of the result is shown Figure 7.

In many cases, the grid lines confounded the process of identifying bubbles, particularly where bubbles only partially overlapped a grid cell. This often caused a single bubble to appear distorted or as multiple bubbles. To avoid this problem, a bubble tracker was implemented. Each newly appearing bubble in a frame was labeled, and subsequent frames were examined to identify the same bubble and give it the same label based on proximity. As an example, if bubble "A" was identified in frame 1, all detected bubbles
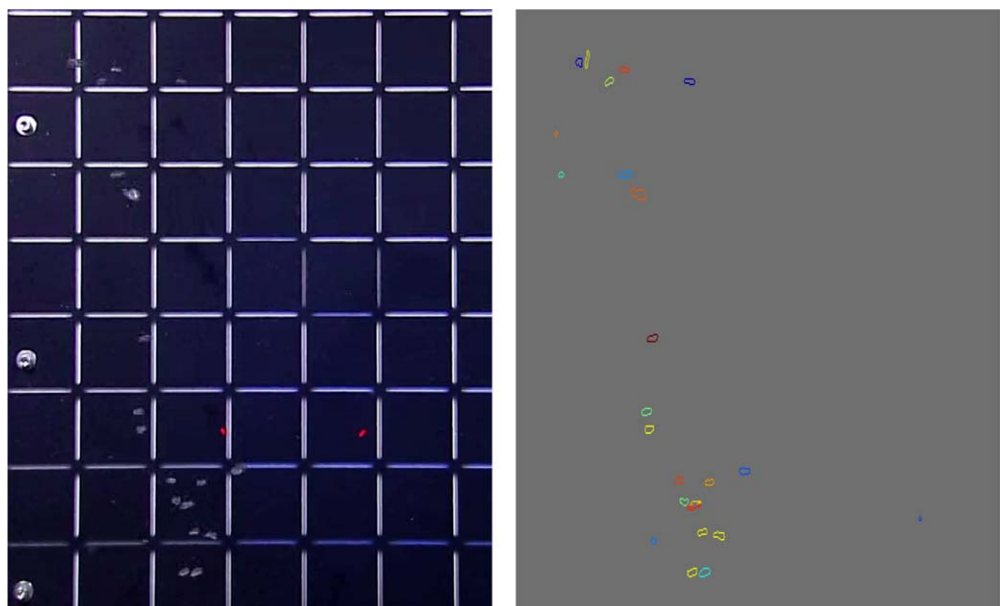

Figure 7. (left) An example of the raw (deinterlaced) video data and (right) the result of the edge detector.
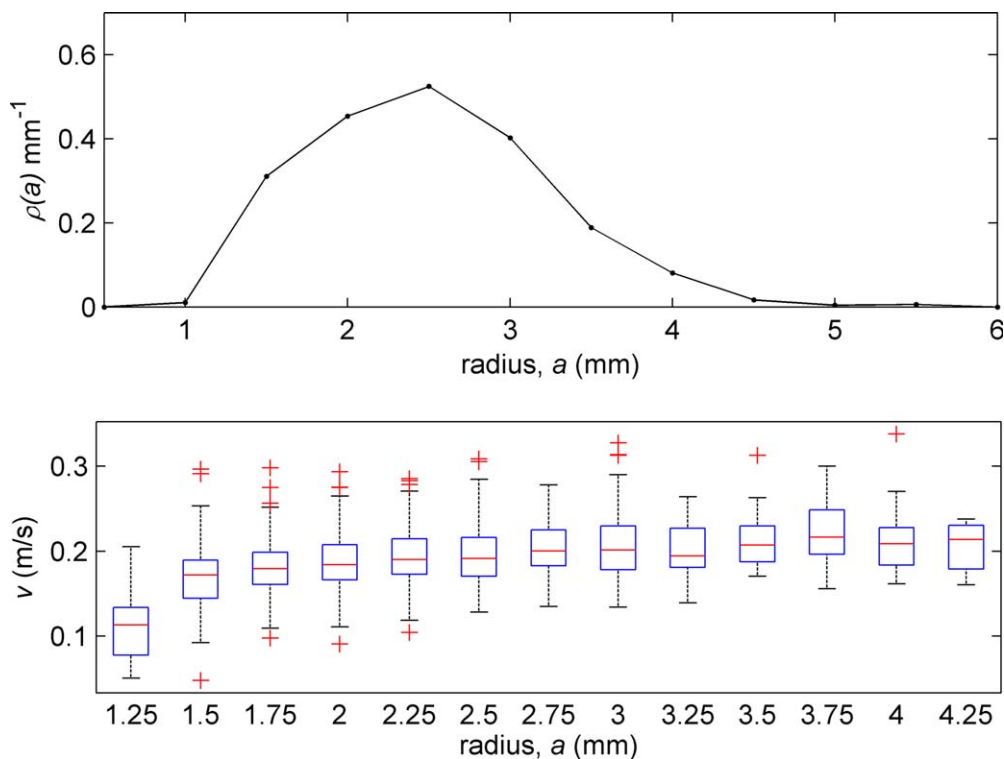
Figure 8. (top) Empirically estimated probability of occurrence, ρ, of observing a bubble of radius a estimated during an ROV dive at the Pascagoula Dome. (bottom) A box plot showing the observed bubble rise velocities (the edges of the box are the 25th and 75th percentiles, and the central mark is the median).

in frame 2 that were not previously labeled were considered as candidate "A"s. The number of bubbles in frame 2 that were within a distance of 20 pixels (1–2 cm) from the location of bubble "A" frame 1 was then identified. If only one bubble met this 20 pixel proximity criterion, then it was assumed that this bubble was identical to the one identified in the previous frame and labeled bubble "A." If more than one bubble was identified within 20 pixels, or if no bubbles were identified, then none of the bubbles in frame 2 were added to the track as bubble "A." This was continued for all bubbles and frames in a video segment. Bubble tracks were ended whenever a bubble was not labeled in two subsequent frames.

To estimate the bubble size distribution and rise velocity, only those tracks including at least 10 frames were used. To calculate the bubble size, an ellipse was fit to the perimeter of the bubble in order to find the median minor and major ellipse axes for the track, b and c, respectively. The volume of the bubble was then calculated as $v = \left(\frac{4}{3}\pi bc^2\right)\left(\frac{7}{8}\right)^3$, where the factor of 7/8 accounts for the size distortion of the bubble due to the measurement geometry. The effective radius of the bubble $a = \left(v / \frac{4}{3}\pi\right)^{1/3}$ was then used in order to generate the size distributions of the bubbles. There is some error in this measurement due to the position of the bubble: if the standard deviation of the bubble position varies by 2 cm in range to the camera, then the associated error in bubble size would be 2.5%. The rise velocity was estimated for each bubble track by dividing the total vertical distance traveled by the total duration of the track. A total of 965 individual bubble tracks were used for the estimates of effective radius and rise velocity in this work. The results of these visual observations suggest bubble radii between 1 and 5 mm (Figure 8, top), consistent with bubble sizes observed previously at deep seeps [*Leifer and MacDonald*, 2003; *Sauter et al.*, 2006; *Sahling et al.*, 2009; *Römer et al.*, 2012], and rise velocities near 20 cm/s (Figure 8, bottom) similar to predicted velocities [*Clift et al.*, 1978].

4. Estimates of Methane Flux From the Seabed for a Single Seep

If the probability density function $\rho(a)$ describing the distribution of bubble sizes, a, is known, then the average acoustic scattering cross section, σ_T, for a bubble seep can be calculated assuming the contributions from individuals add incoherently:
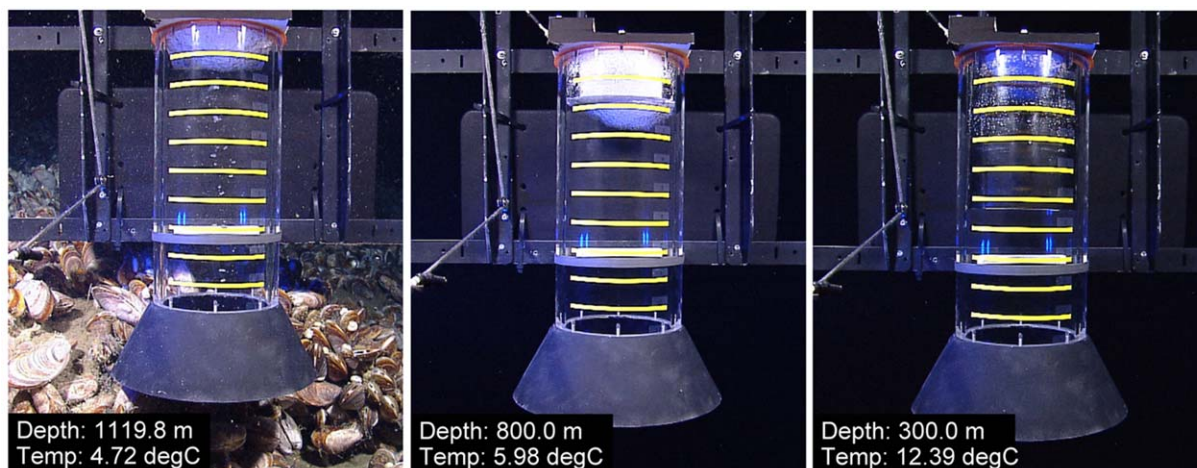
Figure 9. Collection of methane gas from a gas seep at the Pascagoula Dome and behavior of gas and hydrate as the ROV ascended through the water column. From left to right, the images were collected at 22:21:00, 23:02:49, and 23:55:31 (UTC) on 16 April 2012.

$$\sigma_T = \int_0^{a_{max}} \frac{\sigma}{4\pi} \rho(a)da \qquad (2)$$

where a_{max} is the largest bubble size in the plume. The scattering cross section σ is calculated using equation (1) evaluated at the depth of the observation. The volume flow rate, Q, of the seep can be found from

$$Q = N \int_0^{a_{max}} 4/3\pi a^3 v(a)\rho(a)da \qquad (3)$$

where $v(a)$ is the size-dependent rise velocity of the bubbles. N is estimated from the observed TS and average scattering cross section by

$$N = \frac{10^{TS/10}}{\sigma_T} \qquad (4)$$

Q was estimated for the Pascagoula Dome seep visited by the ROV. This seep exhibited a TS at the seabed of -20 dB (Figure 5G*) within a day of the ROV observations (Figures 6–8), based on the same 20 m depth bins used to generate the seep TS profiles with the SBES as described in section 2. Using both the size distribution $\rho(a)$ and average rise velocity $v(a)$ estimated using the grid (Figure 8), the volume flow rate for gas exiting the seabed at this single seep is estimated to be $Q = 3.1 \times 10^{-6}$ m³/s at the in situ depth and temperature of 1120 m and 4.72°C, respectively. Assuming that the bubbles are pure methane, the flow rate Q can be computed from $PV = ZnRT$ where P is the pressure, V is the volume, n is the number of moles, R is the ideal gas constant, T is the temperature, and Z is a compressibility factor accounting for the departure of methane from an ideal gas. At the in situ depth and temperature, Z is estimated from the Peng-Robinson equation of state [*Peng-Robinson*, 1976] to be 0.76, resulting in a flow rate of 0.02 mol/s or 0.32 g/s using a molecular weight of 16.04 g/mol. If the observed conditions were stationary throughout the year, this is equivalent to 1.0×10^7 g/yr. It is important to note that this acoustically derived flow rate estimate could be biased by the presence of other seeps that are within the SBES field of view. In fact, acoustic observations with the higher-resolution MBES showed the presence of four other weaker (by greater than an order of magnitude) seeps. These other seeps are estimated to bias the acoustic TS measurement, and therefore the flow rate, by as much as 10% (see supporting information).

Within a few days of the acoustic and optical measurements, the ROV revisited the same seep and used an optically clear cylinder (closed on top and with a downward-facing funnel on the bottom) to capture
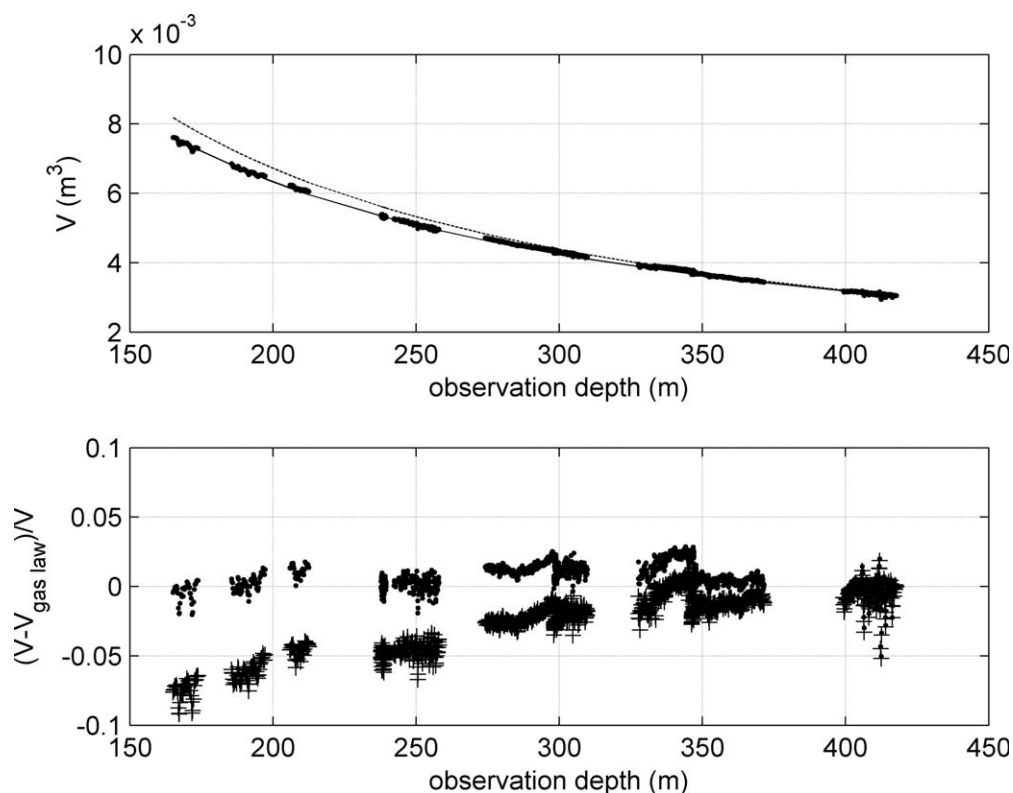
Figure 10. (top) The observed volume of methane gas collected between 165 and 420 m water depth, after methane dissociation (dots), compared with the volume of gas estimated assuming an ideal gas law with 5.6 mol of methane (solid line). (bottom) The difference between the observed volume of methane, V, and the estimated volume of gas assuming an ideal gas law, V_{iso}, divided by the observed volume, V.

methane gas exiting the seep (Figure 9). During gas collection, hydrate formation was observed at the top of the cylinder. The hydrate can be seen as the blue/white material at the top of the funnel in the two left frames of Figure 9. The gas, which appeared to be steadily escaping the seep, was collected for 7 min and 52 s. It should be noted that a few bubbles (i.e., one every several seconds) were observed escaping the seabed outside of the funnel within the camera field of view, but it is estimated that this uncollected gas accounted for less than 1% of the gas escaping the seabed at the location within the field of view of the ROV during the gas collection period.

After 7 min and 52 s of gas collection, the ROV maneuvered away from the seep and began to ascend through the water column (video available in supporting information). Free gas was clearly visible inside the funnel at depths as great as 1000 m, and this volume of gas continued to expand as the ROV ascended. The dissociation depth for methane hydrate in the area of study is estimated to be 610 m using the parameterization of *Tishenko et al.* [2006, equation 24]. It is difficult to determine from the imagery whether a thin hydrate boundary exists between this free gas and the seawater below. It is possible that this free gas originated from hydrate-coated bubbles trapped in the top of the funnel that had coalesced as they expanded due to decreasing hydrostatic pressure as the vehicle ascended.

By the time the ROV reached a depth of 420 m, 1 h, and 14 min after departing the seep, all of the hydrate had dissociated and only free gas and water remained in the funnel. At this and shallower depths, the location of the gas-liquid interface was manually digitized in the recorded imagery of the cylinder to determine the interface location in pixels. The cylinder was constructed with nine graduated markings dividing the cylinder into 10 equal volumes. In each image, the 1st and 9th markings were also manually digitized in order to translate the gas-liquid interface location in pixels into a volume estimate using the known volume of the cylinder (inside radius of 0.080 m and height of 0.38 m). By this process, the volume of gas was recorded for 1679 images between 165 and 420 m water depth (Figure 10). The expansion of the gas with depth and

temperature (measured by the ROV during ascent) was then fit to both an ideal gas law ($PV = nRT$), assuming the system was isothermal, resulting in an estimated 5.6 mol of gas collected over the 7 min and 52 s, and a gas law accounting for Z ($PV = ZnRT$) calculated from the Peng-Robinson equation of state, resulting in an estimated 6.2 mol of gas collected. These estimates were calculated at the deepest observation (420 m) to minimize the effect of methane dissolution into the water column. The observed change in volume with depth between 165 and 420 m is compared to both the ideal gas law and a gas law accounting for methane's compressibility (or Z factor), which varies from $Z = 0.89$ to 0.96 (420 m depth/283 K and 165 m depth/290 K, respectively). Interestingly, the ideal gas law provides a much more accurate fit to the observations, although it should be pointed out that neither model accounts for dissolution at the gas/water interface during the ROV ascent. Over the 7 min and 52 s collection period, and assuming dissolution is negligible, the estimates for flux rate at the observation depth of 1120 m and 277.9 K would be $Q = 2.3 \times 10^{-6}$ m^3/s and $Q = 2.0 \times 10^{-6}$ m^3/s using the ideal gas law and the Peng-Robinson equation of state, respectively. These results are 26% and 35% lower than the acoustic estimate, respectively.

5. Estimates of Methane Flux From the Seabed in the Entire Study Area

In addition to the seep at the Pascagoula Dome described in section 4, several other seeps at the Biloxi Dome and a few km south of the Biloxi Dome (Figure 2) were visited with the ROV in 2012. These ROV dives were not able to perform direct methane capture or measurements with the grid, but did employ two lasers spaced 10 cm apart that were used for low-precision estimates of bubble size (although not bubble size distributions such as those presented in Figure 8).

The characteristics of the bubbles at all seeps visited with the ROV in 2012 were found to be quite different from each other, ranging from the relatively wide distribution of bubble sizes observed at the Pascagoula Dome (Figure 8) to a monodisperse bubble size distribution (i.e., bubbles of a single size only) observed at the site south of the Biloxi Dome (see supporting information). All of the bubbles observed during these ROV dives appeared to have radii between 1 and 5 mm, a size range that is consistent with bubble sizes previously observed by other investigators in similar deep water conditions [e.g., *Leifer and MacDonald*, 2003; *Römer et al.*, 2012]. This constraint on bubble size suggests that it may be possible to predict, perhaps crudely, the flux of gas escaping the seabed using the TS measurements made with the SBES.

To estimate the flux of methane gas escaping the seabed for the entire 2011 survey area, several assumptions must be made. We use each SBES TS measurement from the 2011 survey (41 observations, with TS estimated over a 20 m depth bin at the seabed, see supporting information) to estimate the volumetric flux at the seabed for each individual seep observation. The flux at the seabed is estimated as described in section 4, but without the benefit of ROV observations describing the bubble size distribution and rise velocities. To provide at least some bounds for the flux estimate, it is assumed that the observed seeps had a monodisperse bubble size distribution, and that) the rise velocity of a single bubble was 20 cm/s, similar to that predicted by *Clift et al.* [1978] and to the observations of this study (Figure 8, bottom). The assumption of the monodisperse bubble size distribution, which is used with bubble sizes ranging from 1 to 5 mm radius, is an admittedly crude assumption, but one that is assumed to be better than assuming that the single observed bubble size distribution on the Pascagoula Dome (Figure 8) applies to all seeps in the study area (see images of other seep sites shown in the supporting information). The volumetric flux rate at the seep base for each of the 41 TS observations made with the SBES in 2011 was then converted to a mass flux, accounting for the compressibility factor Z (see supporting information) and then linearly extrapolated to the 357 MBES seep observations under the assumption that the distribution of SBES observations was representative of the entire population of seeps within the study area. This process results in a different total mass flux estimate for the study area for each of the assumed bubble radii between 1 and 5 mm, ranging from 0.0004 to 0.05 Tg/yr (Figure 11).

The total flux rate for the 6000 km^2 area studied here is the equivalent of 0.0008–0.1% of the current estimates for global seabed methane seepage rates, assuming a nominal value for the latter of 50 Tg/yr based on several different estimates [*Hovland et al.*, 1993; *Kvenvolden et al.*, 2001; *Judd*, 2000]. The seeps observed in this study likely constitute only a small fraction of the total gas seepage in the Gulf of Mexico basin. For example, observations of gas seeps, gas hydrate, and chemosynthetic communities associated with gas seeps are widespread across the north-central and north-western region of the Gulf of Mexico in a region
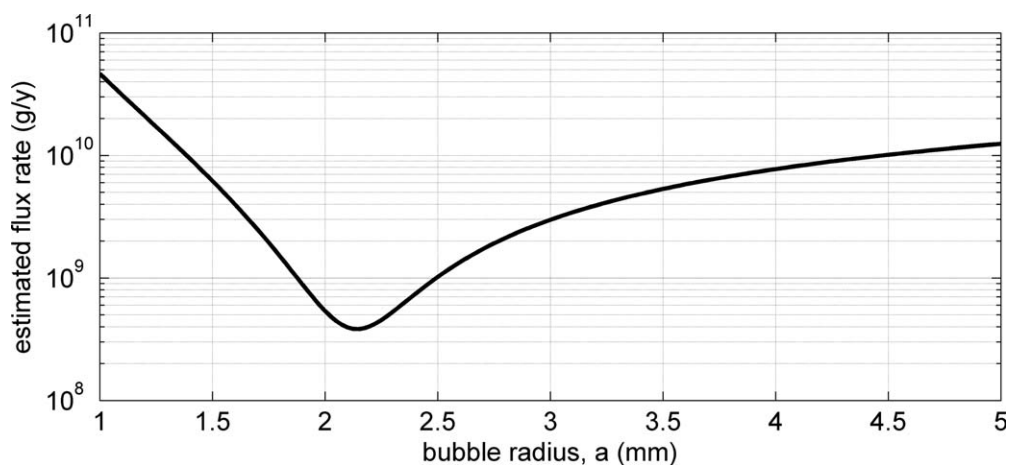
Figure 11. Estimates of methane gas flux at the seabed for the entire study area shown in Figure 2.

far larger than the study area [e.g., *Judd and Hovland*, 2007] (Seabed Fluid Flow, Map 30). These observations are largely nonquantitative in terms of volumetric flux rate, however.

6. Discussion

The acoustic measurements presented here show excellent capacity for making synoptic measurements of seabed gas escapage, a method that several other investigators have taken advantage of [e.g., *Römer et al.*, 2012]. The direct comparison between acoustically derived and directly observed flux from a seep on the Pascagoula Dome show that relatively accurate estimates of gas flux (the direct observations is about 35% lower than the acoustic observation) can be achieved in the deep ocean using shipboard SBES. This comparison neglects the potential influence of smaller, nearby seeps which could result in an overestimate of the acoustic TS and resulting flux estimate, and also neglects methane dissolution in the direct capture experiment which would result in an underestimate of the directly observed flux. Estimates for the seabed flux rate of free gas for the entire study area are much larger, varying by 2 orders of magnitude due to the unknown size distribution of bubbles escaping the seabed.

Additional sources of uncertainty in the flux rate calculations for both the Pascagoula Dome seep and the entire study area may also be present. The acoustic effects of both nonspherical bubbles (note that most observed bubbles had an aspect ratio of 2 or less, see Figure 7 and supporting information) and hydrate coatings on the bubble walls have been neglected. It has been assumed that the gas is comprised exclusively of methane which, if untrue, may change both the formation of a hydrate coating and the dissolution of the bubble during its ascent. Also, the calculations presented here inherently assume that the gas observed to be escaping the seabed during the 2 week time in 2011 represents an accurate "snapshot" of the gas escaping the seabed throughout the year. Some gas seeps have been shown to be episodic [*Greinert*, 2008; *Kannberg et al.*, 2013], and so it is possible that a repeat examination of these seeps would show that some are still present, some are no longer seeping, and some new seeps have appeared. Although it seems reasonable to assume that the flux of escaping gas was not appreciably changing on a regional scale during the survey, information to show that this is the case within the study area is not presently available.

Although the acoustic measurements were effective at identifying the locations and numbers of gas seeps, the use of only a single frequency has resulted in a wide range of values in the resulting flux estimate. The use of multiple frequencies could be used to further constrain this estimate by exploiting the strong frequency-dependence in the bubble target strength. Such a measurement would be novel for a natural methane seep, but wideband acoustic measurements have been made previously for estimating the void fraction of air bubbles under breaking waves [e.g., *Medwin and Brietz*, 1989; *Terrill and Melville*, 2000; *Vagle and Farmer*, 1992], to discriminate between fish species [*Holliday*, 1972; *Thompson and Love*, 1996; *Stanton et al.*, 2010], and to distinguish scattering from turbulence from marine organisms [*Lavery et al.*, 2010].

After addressing the gas escaping the seafloor, the next obvious question is the eventual fate of the methane. This question has not been substantially addressed in this work, but the data presented here do not offer some potential insights into the fate of methane bubbles in this deep water region. Methane is undersaturated in the deep ocean, and clean methane bubbles are expected to lose much of their mass over several tens of meters [*Rehder et al.*, 2002; *McGinnis et al.*, 2006; *Rehder et al.*, 2009]. The observations presented here (Figures 3 and 5) show that these gas seeps are rising several hundreds of meters through the water column. This seems likely to be a result of the suggested impediment to gas transfer provided by a skin of hydrate at the gas-liquid boundary of the bubble, acting to slow the rate of gas transfer [*Rehder et al.*, 2002; *McGinnis et al.*, 2006]. Oil coatings on bubbles have also been suggested as a mechanism for slowing the rate of gas transfer, possibly to a rate sufficiently slow that methane bubbles reach the sea surface [*MacDonald et al.*, 2002; *Solomon et al.*, 2009]. Although we observed tall gas seeps, suggesting some kind of impediment to gas transfer relative to a "clean" bubble, when conducting this work we rarely observed methane bubbles rising above the hydrate stability zone (HSZ), and often the observations did not extend even up to the top of the predicted HSZ. More work is required, however, to determine whether the rising bubbles were undetectable due to acoustic reverberation (or masking) from the deep scattering layer, whether the bubbles rose outside of the SBES and MBES angular field of view, or whether the bubbles substantially dissolved deep within the water column.

References

Burdic, W. S. (1991), *Underwater Acoustic System Analysis*, 2nd ed., pp. 328–331, Prentice Hall, Upper Saddle River, N. J.

Clay, C., and H. Medwin (1977), *Acoustical Oceanography: Principles and Applications*, pp. 194–201 and 236–241, New York: John Wiley & Sons.

Clift, R., J. R. Grace, and M. E. Weber (1978), *Bubbles, Drops and Particles*, pp. 172, Academic, New York.

Dimitrov, L., and V. Dontcheva (1994), Seabed pockmarks in the southern Bulgarian Black Sea zone, *Bull. Geol. Soc. Den.*, 41, 24–33.

Epstein, C. E. P., and M. S. Plesset (1950), On the stability of gas bubbles in liquid-as solutions, *J. Chem. Phys.*, 18(11), 1505–1509.

Feuillade, C., and M. F. Werby (1994), Resonances of deformed gas bubbles in liquids, *J. Acoust. Soc. Am.*, 96(6), 3684–3692.

Foote, K., H. Knudsen, G. Vestnes, D. MacLennan, and E. Simmonds (1987), Calibration of Acoustic instruments for fish density estimation, *ICES Coop. Res. Rep.* 144, 81 pp, International Council for the Exploration of the Sea.

Francois, R. E., and G. R. Garrison (1982), Sound absorption based on ocean measurements: Part I: Pure water and magnesium sulfate contributions, *J. Acoust. Soc. Am.*, 72, 896.

Garcia-Pineda, O., I. MacDonald, B. Zimmer, B. Shedd, and H. Roberts (2010), Remote-sensing evaluation of geophysical anomaly sites in the outer continental slope, northern Gulf of Mexico, *Deep Sea Res., Part II*, 57(21), 1859–1869.

Greinert, J. (2008), Monitoring temporal variability of bubble release at seeps: The hydroacoustic swath system GasQuant, *J. Geophys. Res.*, 113, C07048, doi:10.1029/2007JC004704.

Greinert, J., Y. Artemov, V. Egorov, M. De Batist, and D. McGinnis (2006), 1300-m-high rising bubbles from mud volcanos at 2080 m in the Black Sea: Hydroacoustic characteristics and temporal variability, *Earth Planet. Sci. Lett.*, 244(1–2), 1–15.

Greinert, J., D. F. McGinnis, L. Naudts, P. Linke, and M. De Batist (2010), Atmospheric methane flux from bubbling seeps: Spatially extrapolated quantification from a Black Sea shelf area, *J. Geophys. Res.*, 115, C01002, doi:10.1029/2009JC005381.

Heeschen, K., A. Trehu, R. Collier, E. Suess, and G. Rehder (2003), Distribution and height of methane bubble plumes on the Cascadia Margin characterized by acoustic imaging, *Geophys. Res. Lett.*, 30(12), 1643, doi:10.1029/2003GL016974.

Holliday, D. V. (1972), Resonance structure in echoes from schooled pelagic fish, *J. Acoust. Soc. Am.*, 51, 1322.

Hood, K. C., L. M. Wenger, O. P. Gross, and S. C. Harrison (2002), Hydrocarbon systems analysis of the northern Gulf of Mexico: Delineation of hydrocarbon migration pathways using seeps and seismic imaging, in *Surface Exploration Case Histories: Applications of Geochemistry, Magnetics, and Remote Sensing, AAPG Stud. Geol.*, vol. 48, pp. 25–40, Am. Assoc. of Pet. Geol.

Hopkins, T., and T. Landcraft (1984), The composition and standing stock of mesopelagic micronekton at 27°N 86°W in the eastern Gulf of Mexico, *Contrib. Mar. Sci.*, 27, 143–58.

Hornafius, J., D. Quigley, and B. Luyendyk (1999), The world's most spectacular marine hydrocarbon seeps (Coal Oil Point, Santa Barbar Channel, California): Quantification of emission, *J. Geophys. Res.*, 104, 20,703–20,711.

Hovland, M., A. G. Judd, and R. A. Burke Jr. (1993), The global flux of methane from shallow submarine sediments, *Chemosphere*, 26(1), 559–578.

Judd, A. G. (2000), Geological sources of methane, in *Atmospheric Methane: Its Role in the Global Environment*, edited by M. A. K. Khalil, pp. 280–303, Springer, Berlin.

Judd, A. G. (2004), Natural seabed gas seeps as sources of atmospheric methane, *Environ. Geol.*, 46(8), 988–996.

Judd, A. G., and M. Hovland (2007), *Seabed Fluid Flow: The Impact of Geology, Biology and the Marine Environment*, Cambridge Univ. Press, Cambridge, England.

Kannberg, P. K., A. M. Tréhu, S. D. Pierce, C. K. Paull, and D. W. Caress (2013), Temporal variation of methane flares in the ocean above Hydrate Ridge, Oregon, *Earth Planet. Sci. Lett.*, 368, 33–42.

Kessler, J. D., et al. (2011), A persistent oxygen anomaly reveals the fate of spilled methane in the deep Gulf of Mexico, *Science*, 331(6015), 312–315.

Kvenvolden, K. A., T. D. Lorenson, and W. S. Reeburgh (2001), Attention turns to naturally occurring methane seepage, *Eos Trans. AGU*, 82(40), 457–457.

Lavery, A. C., D. Chu, and J. N. Moum (2010), Measurements of acoustic scattering from zooplankton and oceanic microstructure using a broadband echosounder, *ICES J. Mar. Sci.*, 67(2), 379–394.

Leifer, I., and I. MacDonald (2003), Dynamics of the gas flux from shallow gas hydrate deposits: Interaction between oily hydrate bubbles and the oceanic environment, *Earth Planet. Sci. Lett.*, 210(3), 411–424.

MacDonald, I. R., I. L. R. Sassen, P. Stine, R. Mitchell, and N. J. Guinasso (2002), Transfer of hydrocarbons from natural seeps to the water column and atmosphere, *Geofluids*, *2*, 95–107.

Maini, B. B., and P. R. Bishnoi (1981), Experimental investigation of hydrate formation behaviour of a natural gas bubble in a simulated deep sea environment, *Chem. Eng. Sci.*, *36*(1), 183–189.

Mau, S., D. L. Valentine, J. F. Clark, J. Reed, R. Camilli, and L. Washburn (2007), Dissolved methane distributions and air-sea flux in the plume of a massive seep field, Coal Oil Point, California, *Geophys. Res. Lett.*, *34*, L22603, doi:10.1029/2007GL031344.

McGinnis, D. F., J. Greinert, Y. Artemov, S. E. Beaubien, and A. Wüest (2006), Fate of rising methane bubbles in stratified waters: How much methane reaches the atmosphere?, *J. Geophys. Res.*, *111*, C09007, doi:10.1029/2005JC003183.

Medwin, H., and N. D. Breitz (1989), Ambient and transient bubble spectral densities in quiescent seas and under spilling breakers, *J. Geophys. Res.*, *94*, 12,751–12,759.

Merewether, R., M. S. Olsson, and P. Lonsdale (1985), Acoustically detected hydrocarbon plumes rising from 2-km depths in the Guayamas Basin, Gulf of California, *J. Geophys. Res.*, *90*, 3075–3085.

Peng, D. Y., and D. B. Robinson (1976), A new two-constant equation of state, *Ind. Eng. Chem. Fundam.*, *15*(1), 59–64.

Reeburgh, W. S. (2007), Oceanic methane biogeochemistry, *Chem. Rev.*, *107*(2), 486–513.

Rehder, G., P. W. Brewer, E. T. Peltzer, and G. Friederich (2002), Enhanced lifetime of methane bubble streams within the deep ocean, *Geophys. Res. Lett.*, *29*, 21-1–21-4.

Rehder, G., I. Leifer, P. G. Brewer, G. Friederich, and E. T. Peltzer (2009), Controls on methane bubble dissolution inside and outside the hydrate stability field from open ocean field experiments and numerical modeling, *Mar. Chem.*, *114*(1), 19–30.

Römer, M., H. Sahling, T. Pape, G. Bohrmann, and V. Spieß (2012), Quantification of gas bubble emissions from submarine hydrocarbon seeps at the Makran continental margin (offshore Pakistan), *J. Geophys. Res.*, *117*, C10015, doi:10.1029/2011JC007424.

Sahling, H., et al. (2009), Vodyanitskii mud volcano, Sorokin trough, Black Sea: Geological characterization and quantification of gas bubble streams, *Mar. Pet. Geol.*, *26*(9), 1799–1811.

Sauter, E. J., S. I. Muyakshin, J. L. Charlou, M. Schlüter, A. Boetius, K. Jerosch, E. Damm, J.-P. Foucher, and M. Klages (2006), Methane discharge from a deep-sea submarine mud volcano into the upper water column by gas hydrate-coated methane bubbles, *Earth Planet. Sci. Lett.*, *243*(3), 354–365.

Schneider von Deimling, J., G. Rehder, J. Greinert, D. F. McGinnis, A. Boetius, and P. Linke (2011), Quantification of seep-related methane gas emissions at Tommeliten, North Sea, *Cont. Shelf Res.*, *31*(7), 867–878.

Solomon, E. A., M. Kastner, I. R. MacDonald, and I. Leifer (2009), Considerable methane fluxes to the atmosphere from hydrocarbon seeps in the Gulf of Mexico, *Nat. Geosci.*, *2*(8), 561–565.

Stanton, T. K., D. Chu, J. M. Jech, and J. D. Irish (2010), New broadband methods for resonance classification and high-resolution imagery of fish with swimbladders using a modified commercial broadband echosounder, *ICES J. Mar. Sci.*, *67*(2), 365–378.

Terrill, E. J., and W. K. Melville (2000), A broadband acoustic technique for measuring bubble size distributions: Laboratory and shallow water measurements, *J. Atmos. Oceanic Technol.*, *17*(2), 220–239.

Thompson, C. H., and R. H. Love (1996), Determination of fish size distributions and areal densities using broadband low-frequency measurements, *ICES J. Mar. Sci.*, *53*(2), 197–201.

Tishchenko, P., C. Hensen, K. Wallmann, and C. S. Wong (2005), Calculation of the stability and solubility of methane hydrate in seawater, *Chem. Geol.*, *219*(1), 37–52.

Towler, R. H. (2013), *readEKRaw MATLAB Library (4/4/13)* [Computer software], Alaska Fish. Sci. Cent., Seattle, Wash.

Vagle, S., and D. M. Farmer (1992), The measurement of bubble-size distributions by acoustical backscatter, *J. Atmos. Oceanic Technol.*, *9*(5), 630–644.

Weber, T. C., K. Jerram, and L. Mayer (2012), Acoustic sensing of gas seeps in the deep ocean with split-beam echosounders, in *Proceedings of Meetings on Acoustics*, vol. 17, p. 070057.

Westbrook, G. K., et al. (2009), Escape of methane gas from the seabed along the West Spitsbergen continental margin, *Geophys. Res. Lett.*, *36*, L15608, doi:10.1029/2009GL039191.